Functional Imaging of Spinal Cord Electrical Activity From Its Evoked Magnetic Field

Tomoya Sato*, Yoshiaki Adachi, *Member, IEEE*, Masaki Tomori, Senichi Ishii, Shigenori Kawabata, and Kensuke Sekihara, *Fellow, IEEE*

***Abstract*—This paper investigates dynamic source imaging of the spinal cord electrophysiological activity from its evoked magnetic field by applying the spatial filter version of standardized low-resolution brain electromagnetic tomography (sLORETA). Our computer simulation shows that the sLORETA-based spatial filter can reconstruct the four current sources typically associated with the elicitation of the spinal cord evoked magnetic field (SCEF). The results from animal experiments show that significant changes in the latency and intensity of the reconstructed volume current arise near the location of the artificial incomplete conduction block. The results from the human SCEF show that the SCEF source imaging can visualize the dynamics of the volume currents and other nerve electrical activity propagating along the human spinal cord. These experimental results demonstrate the potential of SCEF source imaging as a future clinical tool for diagnosing cervical spinal cord disorders.**

***Index Terms*—Biomagnetism, spatial filter, spinal cord conduction block, spinal cord evoked magnetic field (SCEF), standardized low-resolution brain electromagnetic tomography (sLORETA).**

I. Introduction

A NERVE conduction block of the cervical spinal cord compressed by intervertebral disks and ligaments may cause myelopathy (such as numbness and paralysis in the limbs). Such spinal cord disorders are common, and the number of patients suffering from these spinal cord disorders exceeds 400 000 in Japan. Unfortunately, because compression and other spinal cord abnormalities found on patient's anatomical images (such as MRI or X-ray images) do not always cause spinal cord disorders, there are no effective methods for accurate diagnosis of spinal cord lesions except for the spinal cord evoked potential (SCEP) measurement [1]. The SCEP measurement can provide functional information on the spinal cord electrical activity, and it has been used for detecting such spinal cord lesions.

Manuscript received December 15, 2008; revised April 20, 2009. Current version published September 16, 2009. This work was supported by Ishikawa High-Tech Sensing Technology Cluster, Ministry of Education, Culture, Sports, Science and Technology, Japan. *Asterisk indicates corresponding author.*

*T. Sato is with the Department of Systems Design and Engineering, Tokyo Metropolitan University, Tokyo 191-0065, Japan (e-mail: sato.tomoya.ieee@gmail.com).

Y. Adachi is with the Applied Electronics Laboratory, Kanazawa Institute of Technology, Kanazawa 921-1331, Japan.

M. Tomori, S. Ishii, and S. Kawabata are with the Department of Orthopedic Surgery, Tokyo Medical and Dental University, Tokyo 113-8519, Japan.

K. Sekihara is with the Department of Systems Design and Engineering, Tokyo Metropolitan University, Tokyo 191-0065, Japan (e-mail: ksekiha@cc.tmit.ac.jp).

Color versions of one or more of the figures in this paper are available online at http://ieeexplore.ieee.org.

Digital Object Identifier 10.1109/TBME.2009.2025506

However, since the SCEP measurement requires inserting an electrode array in the epidural space of a patient, it is a highly invasive diagnostic method [2]. Because highly skilled techniques are needed for this electrode insertion, the SCEP measurement actually has been implemented only at a limited number of hospitals. Accordingly, there has been growing interest in developing biomagnetometers optimized for measuring the spinal cord evoked magnetic field (SCEF), because the SCEF measurement can be carried out mostly noninvasively. A 105-channel biomagnetometer system for human SCEF measurements has been developed recently, and the detection of the SCEF from human subjects has already been reported [3], [4].

In this paper, we investigate dynamic (spatio-temporal) source imaging of the spinal cord electrophysiological activity from its evoked magnetic field, aiming at developing a novel, noninvasive diagnostic tool for cervical spinal cord disorders. Here, we apply a spatial filter imaging algorithm based on standardized low-resolution brain electromagnetic tomography (sLORETA), which was originally developed for brain neuromagnetic source imaging [5]. The sLORETA-based spatial filter is known to have no localization bias and provide 3-D reconstruction of source activities [6], [7].

In this paper, following the brief introduction of the sLORETA-based spatial filter algorithm, in Section III, we present the results of a computer simulation that was conducted to check whether the sLORETA-based spatial filter can reconstruct four sources typically associated with the generation of the SCEF. In Section IV, the spatial filter imaging is applied to SCEF obtained in animal experiments where the animal has an artificial incomplete conduction block of the spinal cord. The results from these animal experiments show that significant changes in the latency and intensity of the reconstructed volume current exist near the location of the artificial incomplete conduction block.

In Section V, we apply the source imaging method to the SCEF measured from a human subject. The results show that the SCEF source imaging can visualize the dynamics of the volume currents and other nerve electrical activities traveling along the human spinal cord. The results of our animal and human experiments clearly indicate that SCEF source imaging can be a promising tool for diagnosing cervical spinal cord disorders.

All experiments in this paper were performed at the Section of Orthopedic Spinal Surgery of Tokyo Medical and Dental University. The animal experiments were performed with the approval of the Tokyo Medical and Dental University Animal Care Committee. The human SCEF experiments were performed with the

approval of the Ethics Committee of Tokyo Medical and Dental University.

II. sLORETA Imaging Algorithm

The sLORETA source reconstruction algorithm was originally proposed in [5]. Since we use its spatial filter modification, the spatial filter version of the sLORETA algorithm is briefly described here, although it was described in [6] and [7]. We define the magnetic field measured by the mth sensor at time t as $b_m(t)$. The entire magnetic measurement at t is expressed as a column vector $\boldsymbol{b}(t)$

$$\boldsymbol{b}(t) = [b_1(t), b_2(t), \ldots, b_M(t)]^T \tag{1}$$

where M is the total number of sensors and the superscript T represents the matrix transpose. The spatial location is represented by the 3-D vector $\boldsymbol{r}$: $\boldsymbol{r} = (x, y, z)$. The source vector at a location $\boldsymbol{r}$ is denoted by

$$\boldsymbol{s}(\boldsymbol{r}, t) = [s_x(\boldsymbol{r}, t), s_y(\boldsymbol{r}, t), s_z(\boldsymbol{r}, t)]^T. \tag{2}$$

We define the outputs of the mth sensor due to a unit-magnitude source at $\boldsymbol{r}$, directed in the x-, y-, and z-direction, as $l_m^x(\boldsymbol{r})$, $l_m^y(\boldsymbol{r})$, and $l_m^z(\boldsymbol{r})$, respectively. These $l_m^x(\boldsymbol{r})$, $l_m^y(\boldsymbol{r})$, and $l_m^z(\boldsymbol{r})$ represent the sensitivity of the mth sensor to a source at $\boldsymbol{r}$ directed in the x-, y-, and z-direction. The three column vectors are denoted as

$$\boldsymbol{l}_x(\boldsymbol{r}) = [l_1^x(\boldsymbol{r}), l_2^x(\boldsymbol{r}), \ldots, l_M^x(\boldsymbol{r})]^T \tag{3}$$

$$\boldsymbol{l}_y(\boldsymbol{r}) = [l_1^y(\boldsymbol{r}), l_2^y(\boldsymbol{r}), \ldots, l_M^y(\boldsymbol{r})]^T \tag{4}$$

$$\boldsymbol{l}_z(\boldsymbol{r}) = [l_1^z(\boldsymbol{r}), l_2^z(\boldsymbol{r}), \ldots, l_M^z(\boldsymbol{r})]^T. \tag{5}$$

The lead-field matrix, which represents the sensitivity of the whole sensor array at $\boldsymbol{r}$, is defined as

$$\boldsymbol{L}(\boldsymbol{r}) = [\boldsymbol{l}_x(\boldsymbol{r}), \boldsymbol{l}_y(\boldsymbol{r}), \boldsymbol{l}_z(\boldsymbol{r})]. \tag{6}$$

The spatial filter reconstructs the source vector at $\boldsymbol{r}$ using

$$\hat{\boldsymbol{s}}(\boldsymbol{r}, t) = \boldsymbol{W}^T(\boldsymbol{r})\boldsymbol{b}(t) \tag{7}$$

where $\hat{\boldsymbol{s}}(\boldsymbol{r}, t)$ is the reconstructed source vector and the matrix $\boldsymbol{W}(\boldsymbol{r})$ is a set of spatial filter weights. The sLORETA filter uses the weights defined in [6] and [7]

$$\boldsymbol{W}(\boldsymbol{r}) = \boldsymbol{G}^{-1}\boldsymbol{L}(\boldsymbol{r})[\boldsymbol{L}^T(\boldsymbol{r})\boldsymbol{G}^{-1}\boldsymbol{L}(\boldsymbol{r})]^{-1/2} \tag{8}$$

where $\boldsymbol{G}$ is the gram matrix defined as

$$\boldsymbol{G} = \int \boldsymbol{L}(\boldsymbol{r})\boldsymbol{L}^T(\boldsymbol{r})d\boldsymbol{r}. \tag{9}$$

In our investigations, when computing the lead-field matrix $\boldsymbol{L}(\boldsymbol{r})$, we do not assume any kind of conductor models, and use the Biot–Savart law, which is derived using the quasi-static approximation of the Maxwell equations [8], [9]. Therefore, the output of the spatial filter in (7) is the density of the total current including both the impressed and volume currents.[1] Also note that the spatial filter version of sLORETA is mathematically equivalent to its original tomographic imaging version, and both versions give exactly the same results. The use of the spatial filter version in our investigation was primarily due to our convenience in the software development.

[1]Strictly speaking, the output of the sLORETA-based spatial filter is a standardized form of the total current density.

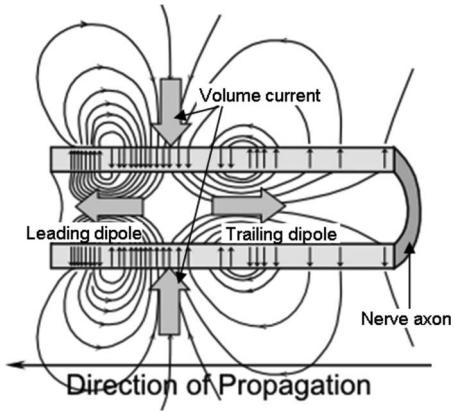

Fig. 1. Schematic illustration of the electrical currents and magnetic field associated with the generation of the SCEF. The halved tube is a model of the nerve axon. The two filled arrows in the axon represent the leading and trailing dipoles traveling in the axon. The other two arrows perpendicular to the axon represent volume currents flowing into the axon.

III. Computer Simulation

The electrophysiological sources propagating in the nerve axon are known to consist of two antidirectional current dipoles [10], which are referred to as the leading and the trailing dipoles [11], [12]. In addition to these two dipole sources, volume currents associated with these dipole sources also produce magnetic fields. The volume current flows from the extracellular milieu to the site between the two dipole sources in the nerve axon, and its direction is perpendicular to the nerve axon. Therefore, we use a source model consisting of four equi-intensity current vectors to express the SCEF sources. These four sources travel with fixed intensity along the nerve axon in the direction of the propagation. They are schematically illustrated in Fig. 1. In the figure, the leading dipole has a direction parallel to the propagation direction, and the trailing dipole has a direction opposite to the propagating direction. Computer simulation was performed to check whether the sLORETA imaging method could resolve these four sources in a realistic measurement condition.

Simulated data at a single time point are generated. The four sources are assumed to exist on a plane located 20 mm below the sensor array, and this plane is defined as $z = 0$ cm. The coordinates and the orientations of these four sources are given in Table I. The first and the second sources are located on the line $x = -10$ mm. Since the propagation direction is assumed to be the positive y-direction, the first source represents the leading dipole and the second source represents the trailing dipole. The third and fourth sources, located on the line $y = 25$ mm, represent the volume currents. We assume the same sensor array as the one used in the animal experiments described in the next section. Here, the sensors are vector sensors, which detect the magnetic field in the three orthogonal field directions. The magnetic field from these four sources was computed using the Biot–Savart law [8], [9]. The contour plots of the generated

TABLE 1
COORDINATES AND ORIENTATIONS OF FOUR SOURCES USED IN COMPUTER SIMULATION

	coordinate (x, y, z) mm	orientation (x, y, z)
First source	$(-10, 45, 0)$	$(0, 1, 0)$
Second source	$(-10, 5, 0)$	$(0, -1, 0)$
Third source	$(-22.5, 25, 0)$	$(1, 0, 0)$
Fourth source	$(-2.5, 25, 0)$	$(-1, 0, 0)$

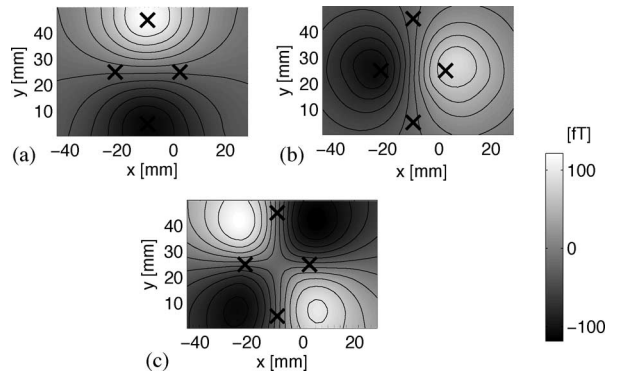

Fig. 2. Contour plots of the magnetic field generated by the source model shown in Fig. 1, which consists of four current sources. (a) x component of the magnetic field. (b) y component of the magnetic field. (c) z components of the magnetic field. The cross marks indicate the locations of the four sources. The field intensity is color-coded according to the color bar.

magnetic field are shown in Fig. 2(a)–(c), where (a), (b), and (c), respectively, represent the x, y, and z components of the magnetic field.

The source reconstruction was performed using the sLORETA-based spatial filter described in the preceding section. The reconstruction region is defined as $-55 \leq x \leq 38, -10 \leq y \leq 60$, and $-15 \leq z \leq 5$ mm. The gram matrix was first computed by integrating the sensor lead field in this region using (9). The source vector was then estimated using (7) and (8). The results of the 3-D source reconstruction are shown in Fig. 3(a)–(c). Fig. 3(a) shows the magnitude distribution of the source vector on the plane $z = 0$ mm. The distribution on the plane $x = -10$ mm is shown in Fig. 3(b). The distribution on the plane $y = 25$ mm is shown in Fig. 3(c). In these results, the positions of maximum intensity of the reconstructed sources are in good agreement with their assumed locations, indicating that the four sources are reconstructed at the correct locations. These results show that the sLORETA method is capable of reconstructing four sources typically associated with the spinal cord electrophysiological activity.

IV. ANIMAL EXPERIMENTS

A. SCEF Measurement

sLORETA imaging was then applied to the SCEF measured from an anesthetized rabbit. A catheter with a balloon tip was inserted into the cervical epidural space, and the cervical spinal cord was artificially compressed by inflating the balloon to make an artificial incomplete conduction block between the fifth cervical vertebra (C5) and the sixth cervical vertebra (C6). The experimental setup is shown in Fig. 4 in which an X-ray image capturing the subject and the sensors is shown together with the location of the artificial conduction block and the reconstruction region. A 24-channel biomagnetometer equipped with vector sensors was used for measuring the cervical SCEF [13]. As shown in Fig. 4, the sensor array was positioned over the neck of the subject.

The sensor array, arranged in a 2×4 matrix structure, can simultaneously measure eight spatial locations, and its coverage is a 6×2 cm region. In these experiments, the position of the sensor array was changed over the cervix ten times to increase the observation area and the density of the observation site. Finally, the magnetic signals were acquired from 64 sites at sensor intervals of 7 and 11 mm in the x- and y-direction, respectively. The data were acquired with a sampling frequency of 40 kHz, and an analog bandpass filter with a bandwidth of 100–5000 Hz was applied. The electrical stimulus was delivered to the spinal cord at the level of the lower thoracic spine using an epidural catheter electrode. A stimulus of 0.03 ms duration and intensity of 5 mA was repeated 3000 times with a repetition interval of 100 ms. The signal was averaged across these 3000 measured trials. We conducted the SCEF measurements twice: once before and once after the artificial incomplete conduction block was induced.

The averaged SCEF recordings are shown in Fig. 5 in which all sensor recordings are displayed, in overlapped fashion. Fig. 5(a) and (b) shows the SCEF waveforms measured before and after the conduction block was made. The electrical stimulus was given at a latency of 0 ms. In Fig. 5, the artifacts caused by the electrical stimulus are observed between 0 and 1 ms of the measured waveforms. In these waveforms, peaks existing after a latency of 1.7 ms are considered to the SCEF signals caused by the stimulus. Comparing the waveforms in Fig. 5(a) with those in Fig. 5(b), one can observe that the amplitudes of the peaks around 3 ms of the latency are significantly reduced in Fig. 5(b). This reduction of the waveform amplitudes is caused by the conduction block and corresponds to the reduction of the volume current intensity, which is argued later.

The measured contour maps of the SCEF at 2.5 ms, as indicated by the broken line in Fig. 5(b), are shown in Fig. 6. The x and y components of the magnetic field, which are tangential to the body surface, are shown in Fig. 6(a) and (b), and the z component of the magnetic field, which is radial to the body surface, is shown in Fig. 6(c). Note that these contour maps are similar to those of the magnetic fields in Fig. 3(a)–(c), and this similarity validates our source model used in the computer simulation.

B. Source Reconstruction Experiments

The source reconstruction was performed in the 3-D region including the subject's spinal cord. In Fig. 4, the dotted square indicates the reconstruction region, which consists of $16 \times 16 \times 16$ voxels. We applied the sLORETA-based spatial filter to the measured SCEF datasets. The source reconstruction results obtained from the SCEF measured after the conduction block was induced are shown in Fig. 7. Here, results at a latency of 2.5 ms were overlaid onto the subject's X-ray image. In this figure, the relative magnitude of the reconstructed sources

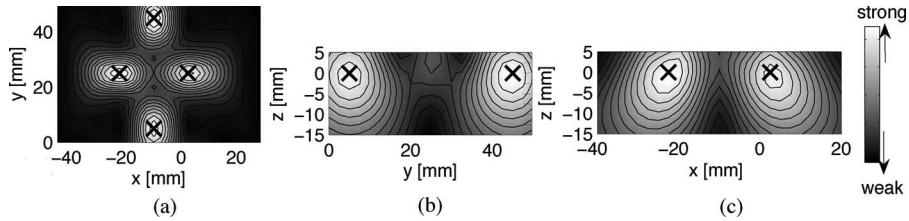

Fig. 3. Results of reconstructing the simulated spinal cord sources using the sLORETA-based spatial filter. (a) Source magnitude distribution on the x–y plane ($z = 0$ mm), on which all the four sources exist. (b) Source magnitude distribution on the y–z plane ($x = -10$ mm), on which the first and second sources exist. (c) Source magnitude distribution on the x–z plane ($y = 25$ mm), on which the third and fourth sources exist. The cross marks represent the source locations. The relative source intensity is color-coded according to the color bar.

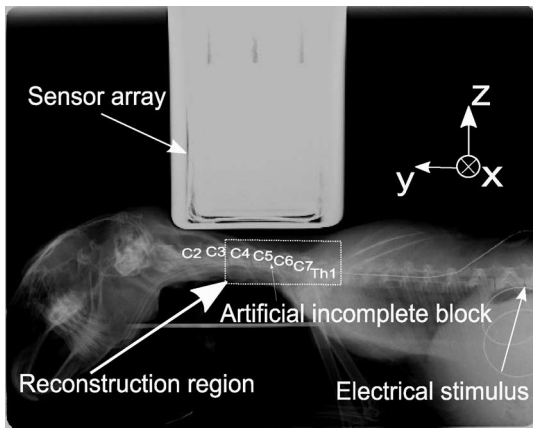

Fig. 4. Animal experiment setup. An X-ray image of the subject and the sensors is shown. The reconstruction region is indicated by the dotted square. The artificial incomplete conduction block was made between the fifth cervical vertebra (C5) and the sixth cervical vertebra (C6). The electrical stimulus was given to the subject's spinal cord at the level of the lower thoracic spine as indicated by the arrow.

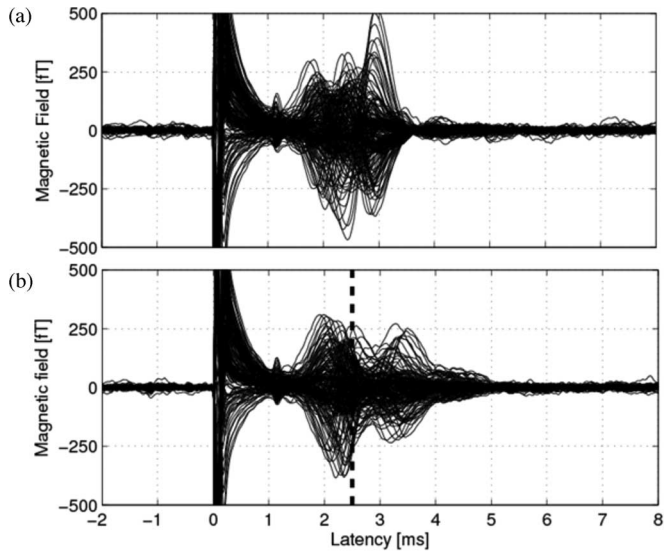

Fig. 5. Sensor recordings of the SCEF obtained in the animal experiments. (a) Recordings taken before the conduction block was induced. (b) Recordings taken after the conduction block was induced. The electrical stimulus was given at a latency of 0 ms. The large magnetic fields between the latencies of 0 and 1 ms are considered artifacts caused by the electrical stimulus, and the peaks after the latency of 1.7 ms are considered to represent the SCEF signals caused by the stimulus.

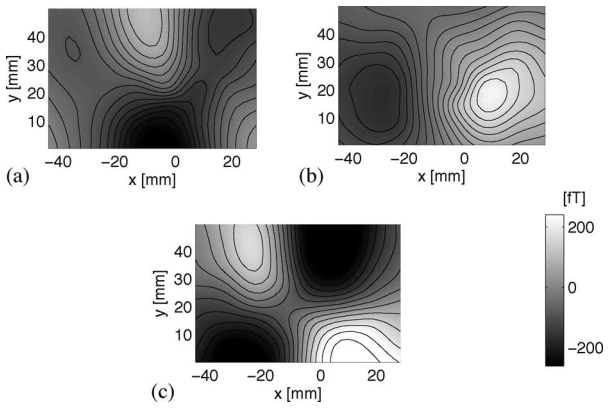

Fig. 6. Measured contour maps of the SCEF at the latency of 2.5 ms indicated by the vertical broken line in Fig. 5. (a) x component of the magnetic field. (b) y component of the magnetic field. (c) z component of the magnetic field. The field intensity is color-coded according to the color bar. The x and y components are tangential to the body surface and the z component is normal to the body surface.

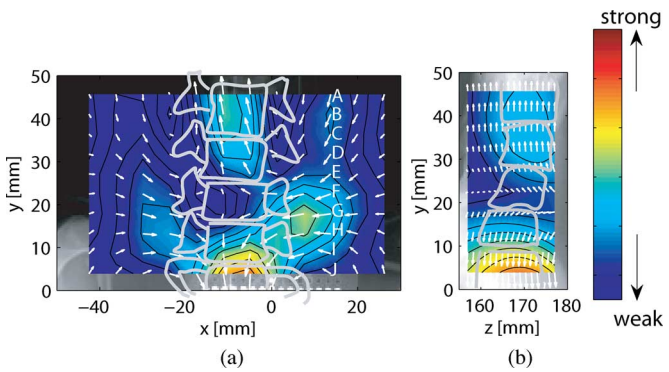

Fig. 7. Results of 3-D reconstruction of the SCEF sources at the latency of 2.5 ms. The results are overlaid onto the subject's X-ray image on which the outline of the subject's spine is superimposed. (a) Source distribution on an x–y plane containing the maximum source activity. (b) Source distribution on a y–z plane containing the maximum source activity. The relative source intensity is color-coded according to the color bar. The arrow indicates the source direction at each voxel. The positive y-direction and the negative y-direction are the cranial and caudal directions, respectively.

is color-coded. The arrow represents the direction of a reconstructed source at each voxel, and its length is proportional to the relative magnitude of the source vector. In these experiments, we reconstructed the x, y, and z components of the source current vector, and the color-coded intensity was obtained using these three components.

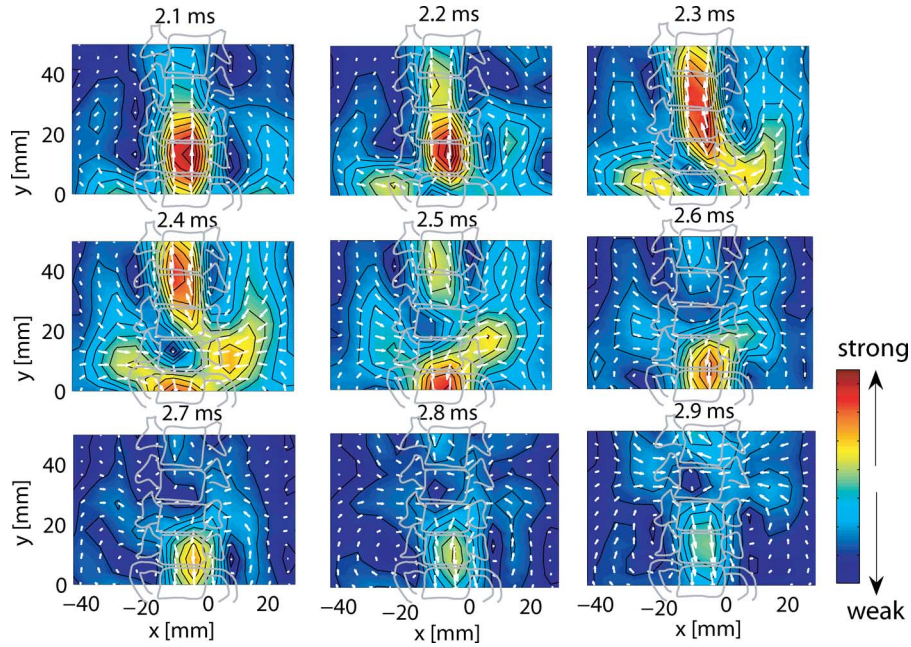

Fig. 8. Reconstructed source distributions on an x–y plane at latencies from 2.1 to 2.9 ms. The outline of the subject's spine is superimposed. The displayed plane is selected as the one that contains the maximum source activity. The artificial incomplete conduction block is located at approximately $y = 30$ mm. The positive y-direction and the negative y-direction are the cranial and the caudal directions, respectively. The relative source intensity is color-coded according to the color bar. The arrow indicates the source direction at each voxel.

The outline of the subject's spine is superimposed onto the X-ray image. In Fig. 7(a), the results on an x–y plane are displayed with the displayed plane chosen as the one that contained the maximum source activity. The results on a y–z plane are shown in Fig. 7(b), and the displayed y–z plane was selected in the same manner. The localized source near $(-10, 40, 170)$ mm can be interpreted as the leading dipole. The trailing dipole is observed near $(-10, 5, 165)$ mm.

Note that, when computing the lead field, we do not use any kind of conductor models, but rather use the formula from the Biot–Savart law, as mentioned previously. Thus, the total current including the volume current is reconstructed as the output of the spatial filter. The two localized sources whose y coordinates are between 10 and 20 mm can be interpreted as the volume currents. The reconstructed source distributions after the blocking in the x–y plane at latencies from 2.1 to 2.9 ms are shown in Fig. 8. In these results, the movement of the sources along the spinal cord toward the subject's head can be observed.

To estimate the temporal change in the intensity of the volume current before and after the block was induced, the time courses at ten selected voxels along the line $x = 14$ mm are plotted. The choice of the line $x = 14$ mm is due to the fact that the maxima of the volume currents travel along this line. These voxels are labeled "A" to "J." The locations and the time courses of these voxels are shown in Fig. 9. Fig. 9(a) and (b) represents the time courses before and after the conduction block was given, respectively. In Fig. 9(a), each time course has a clear peak indicated by an arrow. The latencies of these peaks indicate the instants when the volume current arrived at these voxel locations. On the contrary, in Fig. 9(b), the peaks of the time courses from

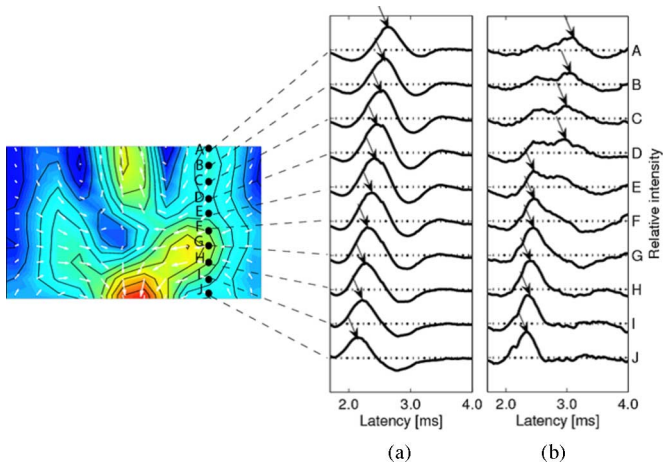

Fig. 9. Time courses of reconstructed source intensity at voxels labeled "A" to "J." (a) Time courses before the conduction block was induced. (b) Time courses after the conduction block was induced. The artificial incomplete conduction block is located between the voxels labeled "D" and "E." The arrow indicates the location of the peak in each time course. The latency of the peak is considered to represent the time when the volume current arrives at that voxel location. The intensity of the peak is considered to represent the intensity of the volume current at that voxel location.

the voxel "G" to "A" become blurred and their amplitudes are lower compared to the corresponding time courses in Fig. 9(a).

The latency of the peaks as well as the intensity of the peaks in Fig. 9(b) is plotted with respect to the y coordinate of these voxels. The results are shown in Fig. 10. The solid circles with broken lines represent the intensity of the peaks, and the open circles with solid lines indicate the latency of the peaks. Note

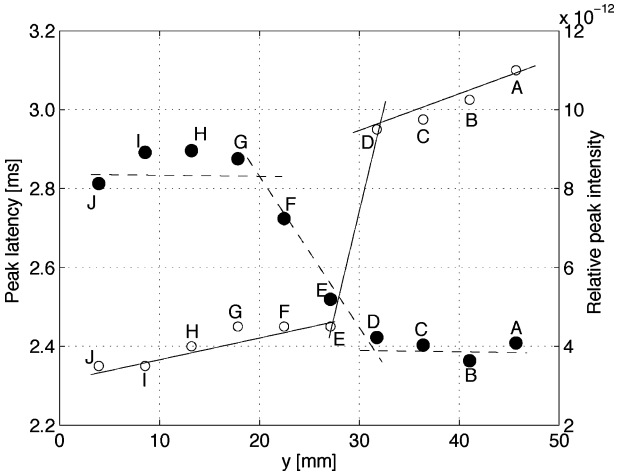

Fig. 10. Latencies and intensities of the peaks in Fig. 9(b) plotted with respect to the y coordinate of the voxels. The plots with the open and solid circles, respectively, show the latency and intensity changes with regard to the voxel y coordinates. The artificial incomplete conduction block is located between the voxels labeled "D" and "E."

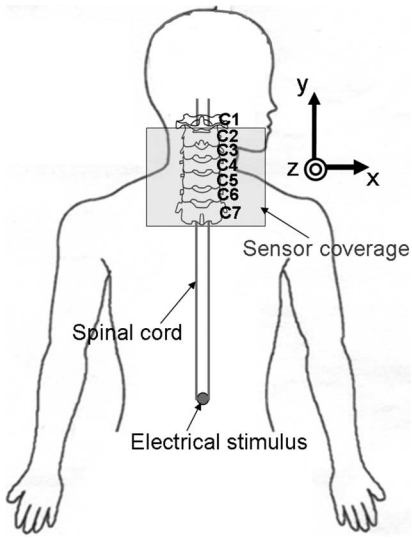

Fig. 11. Schematic view of the human SCEF measurement. An electrical stimulus was applied to the subject's spinal cord at the level of the lower thoracic spine using an epidural catheter-type electrode. The 105-channel biomagnetometer was positioned above the subject's neck.

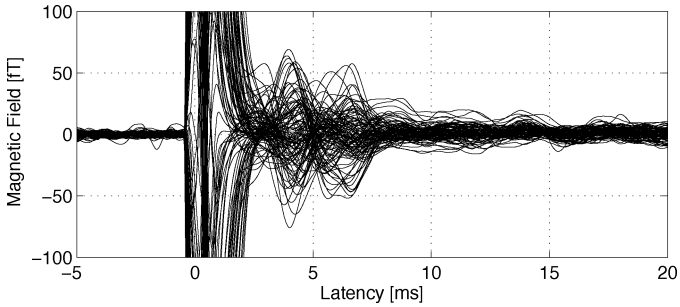

Fig. 12. Sensor recordings of the SCEF from a human subject. The electrical stimulus was given at the latency of 0 ms, and the large magnetic fields between the latencies of 0 and 3 ms are considered stimulus artifacts. The peaks after the latency of 3 ms are considered to represent the SCEF signals corresponding to the electrical stimulus.

that the artificial incomplete block is located at a position with y approximately equal to 30 mm; the position is between voxel "D" and voxel "E." In the latency plot, there is a clear discontinuity between voxel "D" and voxel "E." Also, the intensity significantly decreases between voxel "G" and voxel "D." These results show that significant changes in the latency and intensity of the volume current arise near the location of the incomplete block, and this fact indicates that imaging of the volume current can be a useful tool for diagnosing such spinal cord disorders. Note that similar results can be obtained from the volume currents existing on the opposite side. Also note that we have conducted nine cases of the same animal experiment, and in all cases we have obtained results similar to the representative ones shown in this section.

V. Human SCEF Source Imaging

Spatial filter imaging was applied to the SCEF of a 60-year-old female patient. Although the patient has an atlant-axial subluxation with myelopathy, other parts of her cervical spinal cord were shown to be normal by neurological and image diagnoses. The newly developed 105-channel biomagnetometer was used for measuring the human SCEF [3]. This biomagnetometer is equipped with 35 vector sensors, which are arranged at 7×5 measurement locations covering an 8×9 cm area. The experimental setup is schematically shown in Fig. 11.

A stimulus current with intensity of 4 mA and 0.3 ms duration was applied to the subject's spinal cord at the level of the lower thoracic spine using an epidural catheter-type electrode, and the stimulus was repeated 4000 times at a repetition rate of 20 Hz, with the sampling frequency set to 40 kHz. An analog bandpass filter with a bandwidth of 500–5000 Hz was applied during the data acquisition, and the averaged signal was digitally low-pass filtered with a cutoff frequency of 1.9 kHz. The signal was averaged across the 4000 measured trials. The averaged recordings of the human SCEF are shown in Fig. 12. The latency of 0 ms indicates the time of stimulus application. The peaks after about 3 ms are considered to represent the human SCEF signals caused by the stimulus, while the peaks before about 3 ms are considered stimulus artifacts.

The reconstruction area, indicated by the square in Fig. 11, consists of $16 \times 16 \times 4$ voxels. The voxel intervals are 7.5, 9.5, and 5 mm in the x-, y-, and z-direction, respectively. The reconstructed source distributions on an x–y plane at three latencies from 4.4 to 4.8 ms are shown in Fig. 13. In these results, we can observe the leading and trailing dipoles, as well as the two volume currents propagating toward the subject's head. The source reconstruction results are similar to those of the animal experiments in Fig. 7, and these results show that sLORETA-based imaging can reconstruct the primary and volume currents propagating along the human spinal cord.

VI. Discussion and Summary

Several investigations have been reported regarding the detection of the magnetic signals from brachial nerves and nerve

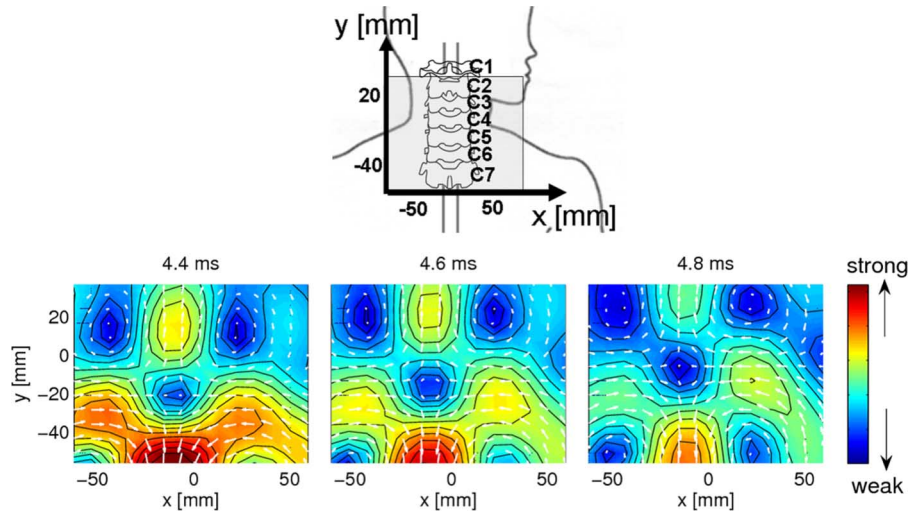

Fig. 13. Reconstructed source distributions on an x–y plane at three latencies from 4.4 to 4.8 ms. The displayed plane was selected as the one that contained the maximum source activity. The relative source intensity is color-coded according to the color bar. The arrow indicates the source direction at each voxel. The positive y-direction and the negative y-direction are the cranial and caudal directions, respectively.

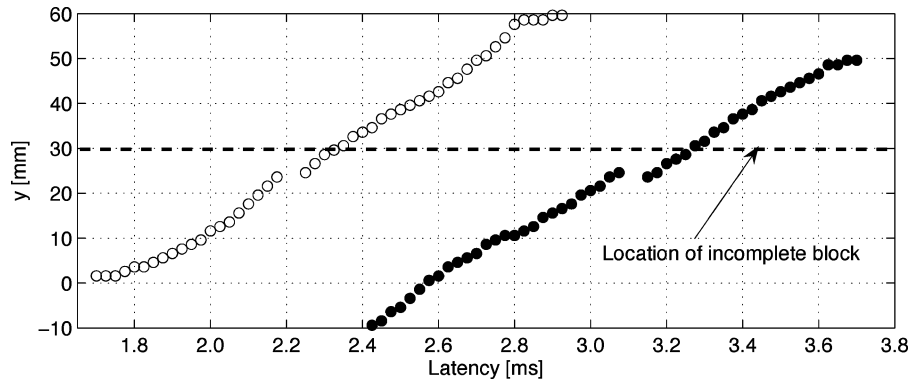

Fig. 14. Estimated y coordinates of the leading and trailing dipoles at each latency. The open circles represent the y coordinate of the leading dipole and the solid circles represent the y coordinate of the trailing dipole. The artificial incomplete conduction block is located at the position with y approximately equal to 30 mm. The small discrepancies existing around 2.2 and 3.2 ms are due to either the switch from the single- to dual-dipole searches or *vice versa*.

root at the cervix [14]–[16]. In these investigations, the single dipole localization method was applied with the half-space volume conductor model [9], and the successful localization of the current dipole along the stimulated nerve fibers was reported [15], [16]. The previous investigations [11], [12] used the dipole localization method applied to the magnetic field generated from rabbits' isolated nerves. In [12], the rabbits' nerves were electrically stimulated in a chamber containing Ringer's solution, and evoked compound action magnetic fields were recorded before and after the incomplete conduction block was introduced by using a vascular clip. The position of the clip was estimated from the conduction velocity changes of the leading dipole. Here, the dipole velocity was estimated by applying the dual-dipole localization to the magnetic field created by the leading and trailing dipoles.

Therefore, in our animal experiments, we first applied the dipole localization method to check whether the incomplete conduction block can be localized. The locations of the leading and the trailing dipoles were estimated through the dual-dipole search. Here, the infinite half-space conductor model [9] was used for the forward calculation. The estimated y coordinates of the leading and the trailing dipoles with respect to time are shown in Fig. 14. In this figure, the white circles represent the y coordinate of the leading dipole and the black circles represent those of the trailing dipole. Here, the positive y-direction and the negative y-direction indicate the cranial and caudal directions, respectively. The artificial incomplete conduction block is located at the position with y approximately equal to 30 mm. As seen in this figure, no significant changes of the conduction velocities of the leading and the trailing dipoles exist at the location of the artificial incomplete conduction block.

In our investigation, we have applied the sLORETA-based spatial filter for imaging the dynamics of human spinal cord electrophysiological activity associated with the SCEF. It should be emphasized that neither specific source model nor the volume conductor model is assumed. Therefore, the spatial filter imaging can visualize the volume current associated with the leading and the trailing dipoles. The primary finding in our animal experiments is that the changes in the conduction velocity and in the intensity of the volume current can detect the location

of the incomplete conduction block. Thus, the visualization of the volume current by using the spatial filter is potentially useful for diagnosing spinal cord disorders.

These volume current sources may also be detected by a multidipole search method. The problem of the dipole search method, however, is the need to specify the number of dipoles. In the case of our SCEF measurements, only at relatively few time points, the sensor field maps show typical dipole or quadrupole field patterns such as the one shown in Fig. 2. Most often, the sensor maps show some intermediate patterns different from these typical field patterns. Therefore, if we apply the dipole search method, we have to select the number of dipoles at each time point, either by visual inspection or by developing other methods to select the number of sources. Our spatial filter imaging does not require determining the number of sources. Moreover, it does not use a high-dimensional search such as that used in multidipole search methods, and it is easier to implement.

We are now investigating the clinical relevance of the proposed SCEF imaging, and more than 100 patients have participated in the study. The results from these patients are now under careful evaluation, and the results of this evaluation will be published in an appropriate clinical journal in near future. The method of applying an electrical stimulus to a patient in Section V requires surgical procedures to insert an epidural electrode proximal to the lower thoracic spine of a patient. This is a fairly invasive method. We have explored the possibility of imaging spinal cord activity from the SCEF evoked by median nerve stimulation, which is virtually noninvasive. Results of this investigation will also be published in the future.

REFERENCES

[1] K. Shinomiya, K. Furuya, R. Sato, A. Okamoto, Y. Kurosa, and M. Fuchioka, "Electrophysiologic diagnosis of cervical OPLL myelopathy using evoked spinal cord potentials," *Spine*, vol. 13, pp. 1225–1233, 1998.

[2] S. Kawabata, H. Komori, K. Mochida, H. Ohkubo, and K. Shinomiya, "Visualization of conductive spinal cord activity using a bio-magnetometer," *Spine*, vol. 27, pp. 475–479, 2003.

[3] Y. Adachi, J. Kawai, M. Miyamoto, G. Uehara, S. Kawabata, M. Tomori, S. Ishii, and T. Sato, "A 105-ch squid magnetometer system for human cervical spinal cord evoked magnetic field measurement," in *Proc. 16th Int. Conf. Biomagn.*, R. Kakigi, Y. Yokosawa, and S. Kuriki, Eds. Sapporo, Japan: Hokkaido Univ. Press, 2008, pp. 24–26.

[4] Y. Adachi, J. Kawai, G. Uehara, H. Ogata, M. Miyamoto, S. Kawabata, and S. Tomizawa, "A SQUID biomagnetometer system for measurement of a human cervical spinal cord evoked field," *Supercond. Sci. Technol.*, vol. 18, pp. 303–307, 2005.

[5] R. D. Pascual-Marqui, "Standardized low resolution brain electromagnetic tomography (sLORETA): Technical details," *Methods Find. Exp. Clin. Pharmacol.*, vol. 24, pp. 5–12, 2002.

[6] K. Sekihara, M. Sahani, and S. S. Nagarajan, "Location bias and spatial resolution of adaptive and non-adaptive spatial filters for MEG source reconstruction," *NeuroImage*, vol. 25, pp. 1056–1067, 2005.

[7] K. Sekihara and S. S. Nagarajan, *Adaptive Spatial Filters for Electromagnetic Brain Imaging*. Berlin, Germany: Springer-Verlag, 2008.

[8] J. C. Mosher, R. M. Leahy, and P. S. Lewis, "EEG and MEG: Forward solutions for inverse methods," *IEEE Trans. Biomed. Eng.*, vol. 46, no. 3, pp. 245–259, Mar. 1999.

[9] J. Sarvas, "Basic mathematical and electromagnetic concepts of the biomagnetic inverse problem," *Phys. Med. Biol.*, vol. 32, pp. 11–22, 1987.

[10] J. P. Wikso, "Biomagnetic sources and their models," in *Advances in Biomagnetism*. S. J. Williamson and L. Kaufman, Eds. New York: Plenum, 1989, pp. 1–18.

[11] Y. Fukuoka, H. Komori, S. Kawabata, H. Ohkubo, K. Shinomiya, and O. Terasaki, "Imaging of neural conduction block by neuromagnetic recording," *Clin. Neurophysiol.*, vol. 113, pp. 1985–1992, 2002.

[12] Y. Fukuoka, H. Komori, S. Kawabata, H. Ohkubo, and K. Shinomiya, "Visualization of incomplete conduction block by neuromagnetic recording," *Clin. Neurophysiol.*, vol. 115, pp. 2113–2122, 2004.

[13] Y. Adachi, G. Uehara, J. Kawai, S. Kawabata, H. Okubo, H. Komori, and H. Kado, "A SQUID biomagnetometer system for measurement of spinal cord evoked magnetic fields," *Supercond. Sci. Technol.*, vol. 14, pp. 1075–1080, 2001.

[14] I. Hashimoto, T. Mashiko, T. Mizuta, T. Imada, Y. Iwase, and H. Okazaki, "Visualization of a moving quadrupole with magnetic measurements of peripheral nerve action fields," *Electroencephalogr. Clin. Neurophysiol.*, vol. 72, pp. 277–280, 1989.

[15] B.-M. Mackert, M. Burghoff, L.-H. Hiss, M. Nordahn, P. Marx, L. Trahms, and G. Curio, "Magnetoneurography of evoked compound action currents in human cervical nerve roots," *Clin. Neurophysiol.*, vol. 112, pp. 330–335, 2001.

[16] B.-M. Mackert, M. Burghoff, L.-H. Hiss, M. Nordahn, L. Trahms, and G. Curio, "Non-invasive magnetoneurography for 3D-monitoring of human compound action current propagation in deep brachial plexus," *Neurosci. Lett.*, vol. 289, pp. 33–36, 2000.

Tomoya Sato received the B.E. degree from Tokyo Metropolitan Institute of Technology, Tokyo, Japan, in 2007, and the M.E. degree from Tokyo Metropolitan University, Tokyo, in 2009.

He is currently with the Department of Systems Design and Engineering, Tokyo Metropolitan University. His current research interests include the neuromagnetic source imaging and the reconstruction methods, especially their application to functional imaging of the spinal cord electrical activity.

Mr. Sato received the Young Investigator Award from the International Conference on Biomagnetism in 2008, Sapporo, Japan. He is a member of the Japan Biomagnetism and Biomagnetics Society.

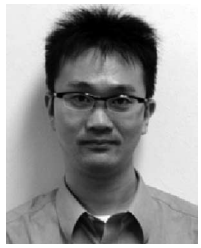

Yoshiaki Adachi (M'99) received the M.E. and Ph.D. degrees from Osaka University, Osaka, Japan, in 1994 and 2007, respectively.

From 1994 to 1997, he was involved in the field of magnetoencephalogram (MEG) measurement with the Electrotechnical Laboratory, Ministry of International Trade and Industry (MITI), Japan. Since 1998, he has been engaged in research and development of the superconducting quantum interference devices (SQUID) and other magnetic flux sensors, their applications, and signal processing at the Applied Electronics Laboratory, Kanazawa Institute of Technology, Kanazawa, Japan.

Dr. Adachi is a member of the Institute of Electrical Engineering of Japan and the Japan Biomagnetism and Biomagnetics Society.

Masaki Tomori received the Bachelor's degree from Tokyo Medical and Dental University, Tokyo, Japan, in 2001.

Since 2005, he has been a Graduate Student at Tokyo Medical and Dental University, where he is currently a Medical Doctor and specializes in orthopedics. His current research interests include the neuromagnetic imaging of spinal cord function.

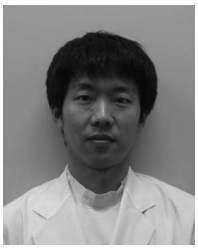

Senichi Ishii received the Bachelor's degree from Tokyo Medical and Dental University, Tokyo, Japan, in 2001.

Since 2005, he has been a Graduate Student at Tokyo Medical and Dental University, where he is currently a Medical Doctor and specializes in orthopedics. His current research interests include the neuromagnetic imaging of spinal cord and peripheral nerve function.

Shigenori Kawabata received the Bachelor's degree from Tokyo Medical and Dental University, Tokyo, Japan, in 1993, and the Ph.D. degree from the Graduate School, Tokyo Medical and Dental University, in 2002.

Since 2003, he has been with the University Hospital of Medicine, Tokyo Medical and Dental University, where he is currently an Assistant Professor at the Section of Orthopaedic Surgery, Graduate School. His current research interests include the spine surgery and the evaluation of spinal cord function.

Kensuke Sekihara (M'88–SM'06–F'09) received the M.S. degree and the Ph.D. degree from Tokyo Institute of Technology, Tokyo, Japan, in 1976 and 1987, respectively.

From 1976 to 2000, he was with the Central Research Laboratory, Hitachi, Ltd., Tokyo, Japan. From 1985 to 1986, he was a Visiting Research Scientist at Stanford University, Stanford, CA. From 1991 to 1992, he was a Visiting Research Scientist at Basic Development, Siemens Medical Engineering, Erlangen, Germany. From 1996 to 2000, he was involved with the "Mind Articulation" Research Project sponsored by Japan Science and Technology Corporation. He is currently a Professor with the Department of Systems Design and Engineering, Tokyo Metropolitan University, Tokyo. His current research interests include the electromagnetic source imaging, reconstruction and inverse methods, multidimensional signal processing, and statistical signal processing, especially their application to functional source imaging. He is the author of a book *Adaptive Spatial Filters for Electromagnetic Brain Imaging* (Springer-Verlag, 2008).

Dr. Sekihara is a member of the IEEE Medicine and Biology Society and the IEEE Signal Processing Society. Dr. Sekihara is a Fellow of the International Society of Functional Source Imaging (ISFSI).